PHOTONICS Research

Fiber optic strain rate sensor based on a differentiating interferometer

Huicong Li,[1,2] Wenzhu Huang,[1,3] Wentao Zhang,[1,2,*] and Jianxiang Zhang[1,2]

[1]State Key Laboratory of Transducer Technology, Institute of Semiconductors, Chinese Academy of Sciences, Beijing 100083, China
[2]College of Materials Science and Opto-Electronic Technology, University of Chinese Academy of Sciences, Beijing 100049, China
[3]Shenzhen Academy of Disaster Prevention and Reduction, Shenzhen 518003, China
*Corresponding author: zhangwt@semi.ac.cn

Received 6 July 2022; revised 16 September 2022; accepted 19 September 2022; posted 19 September 2022 (Doc. ID 468283); published 28 October 2022

Strain rate is an important basic physical parameter in the fields of deformation observation, geodetic measurement, and geophysical monitoring. This paper proposes a novel fiber optic strain rate sensor (FOSRS) that can directly measure the strain rate through a differentiating interferometer that converts the strain rate to the optical phase. The sensing principle, sensitivity, resolution, and dynamic range of the proposed FOSRS are theoretically analyzed and verified by experiment. The experimental results show that the developed FOSRS with a 12.1 m sensing fiber has a flat sensitivity of 69.50 dB, a nanostrain rate (nε/s) resolution, and a dynamic range of better than 95 dB. An ultrahigh static resolution of 17.07 pε/s can be achieved by using a 25.277 km sensing fiber for long baseline measurements. The proposed method significantly outperforms existing indirect measurement methods and has potential applications in geophysical monitoring and crustal deformation observation.

https://doi.org/10.1364/PRJ.468283

1. INTRODUCTION

The strain rate, which is defined as the derivative of the strain with respect to the time in physics, reflects the change process of the strain with time. In earthquake engineering, the dynamic response of the structure to seismic loads is related to the strain rate [1,2], and the seismic design needs to consider the strain rate effect of the structure [3,4]. In geophysics and seismology, the strain rate is important for geodetic strain measurement, tectonic study, and crustal deformation observation. This is helpful in studying aseismic deformation [5], seismicity [6], and seismic hazard assessment [7].

There are several indirect ways to measure the strain rate. For the strain rate field of crustal movement, the displacements or velocities of ground observation stations are directly obtained through global positioning system (GPS) [8,9] or interferometric synthetic aperture radar (InSAR) [7], and mathematical methods or physical models are used to construct the strain rate fields [9,10]. The observation area of this method is hundreds of kilometers and requires as complete geological data as possible, and the calculation method and correction model are complicated [11]. Distributed acoustic sensing (DAS), a novel technology for geophysical and seismological research in recent years, can analyze ground motion information by measuring the strain rate of optical cables [12]. DAS can interrogate the phase change of the backscattered light at each spatial sampling location (channel) through optical pulses and calculate the strain rate in combination with the corresponding gauge length of the channels [13–15]. In fact, the strain rate measurement of DAS is the average result of multiple channels, and there is an overlap of strain rates probed for successive DAS traces. These methods are important means of geodetic measurement and geophysical exploration, but none of them can realize the direct measurement of the strain rate, and it is difficult to process and analyze a large amount of recorded data.

Sensors that can directly measure the strain rate have been reported and are intended for the active control of high-rise buildings or structures. Lee and O'Sullivan presented a piezoelectric strain rate sensor [16], and Juston and Bauer developed a variable reluctance transformer (VRT) strain sensor [17]. However, both piezoelectric and VRT strain rate sensors are electromagnetically sensitive, and they are limited by the piezoelectric material and nonlinearity between the sensitivity and strain amplitude, respectively. In comparison, fiber optic sensing technology with the advantage of anti-electromagnetic interference has been applied in structure health monitoring [18], crustal deformation [19,20], and seismic wave detection [21]. Most importantly, the optical fiber itself is sensitive to strain and can directly sense strain and strain rate, which makes the measurement more reliable. Lo and Sirkis first presented a fiber optic strain rate sensor (FOSRS) based on Doppler wavelength shifts and proved the feasibility of fiber optic sensing for strain

rate measurement [22]. These strain rate sensors, which can directly measure the strain rate, have a huge advantage in that the measured signal has a higher signal-to-noise ratio (SNR) than the differential of the strain. Regrettably, further research on sensitivity, resolution, and dynamic range is lacking. Moreover, there is no sensor for the direct measurement of the strain rate in geophysics and seismology.

In this paper, we propose an FOSRS that is based on a differentiating interferometer. Using the differential optical path structure of the differentiating interferometer, we perform simple, direct, and high-resolution measurements of the strain rate through a single sensing fiber to apply the FOSRS for geophysical monitoring and crustal deformation observation. The principle of strain rate sensing, the method of low-coherence interference, and the demodulation of differentiating interferometers are introduced in detail. This is the first systematic study of strain rate sensitivity, resolution, and dynamic range. The experimental results show that, for an FOSRS with a 12.1 m sensing fiber, the strain rate sensitivity is consistent in the working frequency band, the resolution reaches the nanostrain rate (nε/s), and the dynamic range is above 95 dB. Using a sensing fiber as long as 25.277 km, an ultrahigh static strain rate resolution of 17.01 pε/s can be achieved, indicating that the FOSRS has potential in geophysics and seismology.

2. THEORETICAL ANALYSIS OF THE STRAIN RATE SENSOR

A. Sensing Principle

The system setup of the FOSRS is shown in Fig. 1. The sensing fiber between the 1 × 2 coupler and the Faraday rotator mirror (FRM) is used to be fully coupled to the ground and to sense the strain rate of crustal deformation. When the sensing fiber senses the strain rate, its physical length changes at a speed. Then, the strain rate of the sensing fiber is defined as

$$\dot{\varepsilon}(t) = \frac{\mathrm{d}\varepsilon(t)}{\mathrm{d}t} = \int \frac{\mathrm{d}}{\mathrm{d}t}\left(\frac{\mathrm{d}l}{L}\right) = \int \frac{\mathrm{d}v}{L}, \tag{1}$$

where $\varepsilon(t)$ is the strain of the sensing fiber, L is the baseline length of the sensing fiber, and v is the moving speed of the sensing fiber.

The strain rate reflects the speed of the deformation and strain accumulation process. Thus, the accumulated strain causes changes in the optical path. Because of the stretch of the optical fiber, not only the baseline length but also the refractive index of the sensing fiber changes. The refractive index change of the optical fiber can be described by the Butter and Hocker relationship [23]. Then, the change in the optical path is a function of the change in the baseline length, which is expressed as

$$\Delta L_{\mathrm{opt}}(t) = \left\{1 - \frac{n^2}{2}[(1-\sigma)p_{12} - \sigma p_{11}]\right\} n\Delta L(t) = \xi n \Delta L(t), \tag{2}$$

where $\Delta L(t)$ is the change in the baseline length of the sensing fiber, n is the refractive index of the optical fiber core, σ is the Poisson's ratio of the optical fiber, p_{11} and p_{12} are the two components of the isotropic strain-optic tensor, and ξ is the strain-optic coefficient.

Therefore, the optical phase difference in the sensing fiber can be expressed as

$$\varphi(t) = \frac{4\pi\xi n L}{\lambda_0}\varepsilon(t), \tag{3}$$

where λ_0 is the central wavelength of the amplified spontaneous emission (ASE) source.

In our FOSRS, an unbalanced Mach–Zehnder interferometer (MZI) and an FRM form a differentiating interferometer [24]. The two light beams entering the MZI from the 3 × 3 coupler have a time difference when they reach the sensing fiber due to the unequal arm length difference of the MZI. The time difference is introduced by the arm length difference of the MZI and is expressed as

$$T = \frac{n(L_D - L_0)}{c}, \tag{4}$$

where c is the speed of light in the vacuum, L_D is the length of the delay fiber, L_0 is the length of the MZI's short arm, and $L_D \gg L_0$.

When the two light beams in MZI pass through the sensing fiber, they are both subjected to phase modulation caused by the strain rate. Because the two light beams are modulated at different times by the strain rate, the optical phase difference of

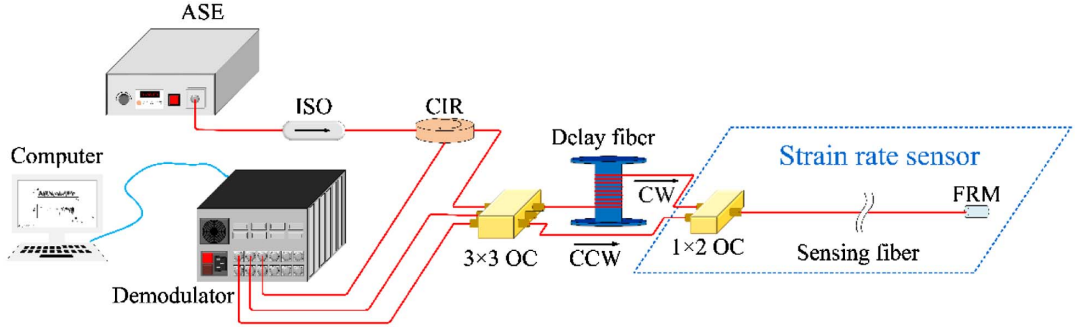

Fig. 1. Fiber optic strain rate sensor system. ASE, amplified spontaneous emission light source; ISO, isolator; CIR, circulator; 3 × 3 OC, 3 × 3 optical coupler; 1 × 2 OC, 1 × 2 optical coupler; FRM, Faraday rotator mirror. Demodulator integrates photodetectors, analog input modules, and embedded controllers. Red and blue lines represent optical fibers and communication cables, respectively.

the light beam that reaches the sensing fiber first is $\varphi(t)$, and the optical phase difference of the light beam that reaches the sensing fiber later is $\varphi(t+T)$. Then, they are reflected by the FRM, enter the MZI, and interfere at the 3 × 3 coupler. Note that only beams passing through the same optical path and in opposite directions can interfere. That is, only the light beam that completes the clockwise (CW) transmission and the light beam that completes the counterclockwise (CCW) transmission satisfy the interference condition. The phase of the interference light can be expressed as [24]

$$\psi = \varphi(t) - \varphi(t+T) = T\frac{\mathrm{d}\varphi(t)}{\mathrm{d}t}. \tag{5}$$

It can be seen from Eq. (5) that the phase of the interference light is the difference between the phases modulated by the strain rate. When the time difference is extremely small, there is a linear correlation between the phase of the interference light and the differential phase modulated by the strain rate. Therefore, through the optical path structure of the differentiating interferometer, the direct relationship between the measurable optical phase and the strain rate is constructed. Combining Eqs. (1)–(5), the strain rate measured by the sensing fiber can be demodulated by the phase of the interference light and is expressed as

$$\dot{\varepsilon}(t) = \frac{c\lambda_0}{4\pi n^2 \xi L(L_D - L_0)}\psi. \tag{6}$$

B. Low-Coherence Interference and Demodulation

FOSRS uses a low-coherence ASE light source that has a broad light spectrum. According to the principle of low-coherence interference and ensemble theory, the time-averaged light intensity when two light beams interfere is [25]

$$\begin{aligned} I(l_{\mathrm{opt}}) &= \langle |E_1(t) + E_2(t + l_{\mathrm{opt}}/c)|^2 \rangle \\ &= I_1 + I_2 + 2\sqrt{I_1 I_2}\,\mathrm{Re}[\gamma(l_{\mathrm{opt}}/c)], \end{aligned} \tag{7}$$

where $I_1 = \langle |E_1(t)|^2 \rangle$ and $I_2 = \langle |E_2(t + l_{\mathrm{opt}}/c)|^2 \rangle$ are the light intensities of the light beams that interfere with each other, $\gamma(l_{\mathrm{opt}}/c)$ is the complex degree of coherence, and l_{opt} is the total optical path difference when the two light beams are interfering and is expressed as

$$l_{\mathrm{opt}} = 2[\Delta L_{\mathrm{opt}}(t) - \Delta L_{\mathrm{opt}}(t+T)], \tag{8}$$

where $\Delta L_{\mathrm{opt}}(t)$ and $\Delta L_{\mathrm{opt}}(t+T)$ are the optical path differences in the sensing fiber. $\gamma(l_{\mathrm{opt}}/c)$ in Eq. (7) is related to the spectrum distribution of the ASE light source. Assuming that the spectral distribution of the ASE light source is a rectangular spectrum, $\gamma(l_{\mathrm{opt}}/c)$ can be simplified as $\mathrm{sinc}(\pi \Delta v l_{\mathrm{opt}}/c)\exp(j2\pi v_0 l_{\mathrm{opt}}/c)$ [26]. Here, Δv and v_0 are the spectral width and central frequency of the ASE light source, respectively. However, the spectral distribution of the ASE light source is not an ideal rectangle, and we think that the amplitude of $\gamma(l_{\mathrm{opt}}/c)$ is close to the form of $\mathrm{sinc}(\pi \Delta v l_{\mathrm{opt}}/c)$ without much deviation. We define a symbol $G(l_{\mathrm{opt}})$ to represent the amplitude of $\gamma(l_{\mathrm{opt}}/c)$. Therefore, Eq. (7) can be expressed as

$$\begin{aligned} I(l_{\mathrm{opt}}) &= I_1 + I_2 + 2\sqrt{I_1 I_2}G(l_{\mathrm{opt}})\exp(j2\pi l_{\mathrm{opt}}/\lambda_0) \\ &= I_1 + I_2 + 2\sqrt{I_1 I_2}G(l_{\mathrm{opt}})\exp(j\psi). \end{aligned} \tag{9}$$

When the FOSRS is static, l_{opt} is zero, I_1 is equal to I_2, and $G(l_{\mathrm{opt}})$ reaches the maximum of 1. When the FOSRS measures the strain rate signal, l_{opt} is not zero, and the light intensity is related to the value of $G(l_{\mathrm{opt}})$. Considering that the light beams without interference contribute to the background signal I' of the photodetector (PD), the light intensity detected by the PD is

$$\begin{aligned} I &= I' + I_1 + I_2 + 2\sqrt{I_1 I_2}G(l_{\mathrm{opt}})\cos(\psi) \\ &= D + A\cos(\psi), \end{aligned} \tag{10}$$

where $D = I' + I_1 + I_2$ represents the DC component of the signal, and $A = 2\sqrt{I_1 I_2}G(l_{\mathrm{opt}})$ represents the AC component of the signal.

A demodulation algorithm based on a 3 × 3 coupler is used to demodulate the phase of the interference light. Three PDs are used to detect the optical signals, and their optical powers are expressed as

$$\begin{aligned} P_1 &= D_1 + A_1\cos(\psi), \\ P_2 &= D_2 + A_2\cos(\psi + \theta), \\ P_3 &= D_3 + A_3\cos(\psi - \theta), \end{aligned} \tag{11}$$

where D_1, D_2, and D_3 are DC components; A_1, A_2, and A_3 are AC components; and θ is $2\pi/3$ in theory, which is determined by the performance of the 3 × 3 coupler. Through an arctangent calculation, the phase in Eq. (11) can be demodulated.

A simulation is carried out to prove that the demodulation algorithm based on a 3 × 3 coupler can be used for the low-coherence interference of the FOSRS. The simulation parameters are listed in Table 1. A light source with a rectangular optical spectrum is simulated. Demodulating the three detection signals shown in Fig. 2(a), the FOSRS measures a simulated strain rate with an amplitude of 1 mε/s and demonstrates it with a phase, as shown in Fig. 2(b).

C. Performance Analysis

In this section, we systematically study the strain rate sensitivity, resolution, and dynamic range of the FOSRS.

Table 1. Simulation Parameters of FOSRS

Parameter	Symbol	Value
Central wavelength	λ_0	1545 nm
Spectral width	Δv	4 THz
Strain-optic coefficient	ξ	0.78
Refractive index	n	1.4682
Length of the delay fiber	L_D	5 km
Length of the sensing fiber	L	10 m
Length of MZI's short arm	L_0	1 m
DC of PD signals	D_i $(i = 1, 2, 3)$	1 μW
AC of PD signals	A_i $(i = 1, 2, 3)$	$0.5\,\mathrm{sinc}(\pi \Delta v l_{\mathrm{opt}} c)$ μW

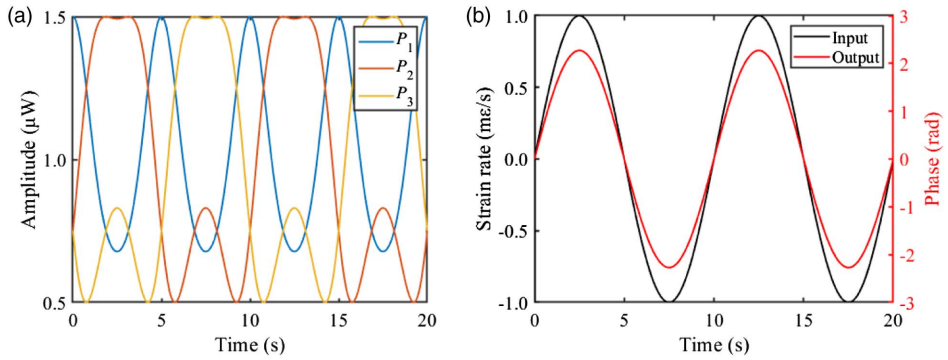

Fig. 2. Demonstration of (a) three detection optical signals and (b) simulated strain rate and phase.

1. Sensitivity

The transfer function between the strain rate and output phase of the interference light is described with a Laplace transform:

$$H(s) = \frac{\psi(s)}{\varepsilon(s)s} = \frac{4\pi n^2 \xi L(L_D - L_0)}{c\lambda_0}. \tag{12}$$

This is the strain rate sensitivity of the FOSRS, which shows that the strain rate has a linear relationship with the phase of the interference light. The strain rate sensitivity is not a function of signal frequency, indicating that its amplitude is consistent over any working frequency band. To improve the sensitivity of the FOSRS, we can increase the baseline length of the sensing fiber, increase the length of the delay fiber, and adopt a light source with a short central wavelength.

2. Resolution

The phase noise floor of the proposed FOSRS determines the limitation of the strain rate resolution. The relative intensity noise (RIN) of the ASE light source is one of the most important factors that limit the resolution of FOSRS and is induced by the random beat of different frequencies of the ASE light source. In some broadband light source systems, especially in the study of fiber optic gyroscopes (FOGs) [27–29], the RIN is also of particular concern. Considering the equivalent phase noise of the RIN, derived from Appendix A, the minimum measurable strain rate is

$$\dot{\varepsilon}_{\min(\mathrm{RIN})} = \frac{10^{\psi_{\mathrm{RIN}}/20} c\lambda_0}{4\pi n^2 \xi L(L_D - L_0)}, \tag{13}$$

where ψ_{RIN} is the power spectral density (PSD) of the equivalent phase noise of the RIN, which is related to the performance of the coupler and the demodulation method.

3. Dynamic Range

The dynamic range of the proposed FOSRS can be analyzed by inferring the maximum measurable strain rate. The optical path difference described in Eq. (8) should be less than the coherence length of the ASE light source; otherwise, the light beams cannot interfere. A low-coherence light source has a coherence length of $\lambda_0^2/\Delta\lambda$ in theory. Therefore, the maximum measurable amplitude of the strain rate is

$$\dot{\varepsilon}_{\max} < \frac{c\lambda_0^2}{2\xi n^2 (L_D - L_0) L\Delta\lambda}. \tag{14}$$

When the RIN determines the resolution limitation of the strain rate, combined with Eq. (13), the theoretical dynamic range of the FOSRS can be expressed as

$$\mathrm{DR} = 20\lg\left(\frac{2\pi\lambda_0}{10^{\psi_{\mathrm{RIN}}/20}\Delta\lambda}\right). \tag{15}$$

The dynamic range is mainly related to the central wavelength, spectral width, RIN of the light source, demodulation algorithm, and performance of the coupler. Note that this applies only to static measurement. In dynamic measurement, the maximum measurable strain rate is affected by total harmonic distortion (THD), not as described by Eq. (15). The dynamic range in dynamic measurement is smaller than that in static measurement.

3. EXPERIMENTAL RESULTS AND DISCUSSION

A. Experimental Setup

The experimental setup of the FOSRS is the same as shown in Fig. 1. The ASE light source (Lightcomm) in the FOSRS system has a central wavelength of 1545 nm and a bandwidth of ~33.377 nm. The developed MZI has a delay fiber with a length of 4.653 km and a short arm with a length of 106.5 cm. To apply the strain rate to the sensing fiber, we wind the sensing fiber with a length of 12.1 m around a piezoelectric transducer (PZT). The optical fibers of MZI and sensing fiber both adopt the SMF-28 type of Corning Inc. A function generator (Tektronix AFG3102) is used to input a voltage and drive the PZT to stretch the sensing fiber, which in turn induces a change in the strain of the sensing fiber. Through the FOSRS, the output phase represents the speed of fiber stretching—that is, the strain rate of the sensing fiber can be measured. The sensing fiber can be stretched 0.14 μm per 1 V voltage.

B. Sensitivity Calibration

To calibrate the strain rate sensitivity of the FOSRS, some sine voltage signals with different frequencies f and amplitudes U are applied to the PZT and stretch the sensing fiber. Then, the strain rate measured by the FOSRS is

$$\dot{\varepsilon} = \frac{0.14 \times 10^{-6} U}{12.1} \cdot 2\pi f \sin(2\pi f t). \tag{16}$$

According to Eq. (12), the strain rate sensitivity is calibrated, and the result is shown in Fig. 3. The sensitivity of the FOSRS is measured from 0.1 Hz to 1 kHz, which is almost flat and has the same flat trend as the theoretical sensitivity curve. This result proves that the FOSRS has the same response to the strain rate in any working frequency band. The average sensitivity measured in the experiment is 69.50 dB in a frequency band of 0.1 Hz to 1 kHz, and its maximum fluctuation is 0.61 dB. This is a difference of 1.32 dB between the average measured sensitivity and the theoretical sensitivity of 68.19 dB. From the perspective of measurement, the difference mainly comes from the errors introduced by the length measurement of the optical fibers, wavelength changes of the ASE light source, and fiber stretch of the PZT. We think that this difference is permissible.

C. Resolution Test

Any disturbance of ambient noise affects the strain rate resolution of the proposed FOSRS, especially the inevitable temperature effects and unwanted vibrations. To research the strain rate resolution, we carried out a test in a basement with a relatively stable temperature and less vibration interference. The MZI, PZT, and FRM are placed in a sealed box with vibration, sound, and temperature isolation.

The 1 min phase is recorded, and its PSD is shown in Fig. 4 with a black line. Some noise peaks between 20 and 40 Hz result from ambient variations. On the whole, the phase noise floor is almost flat and less than −105 dB between 0.1 Hz and 10 kHz. The phase noise floor at 1 kHz is −106.5 dB. Using the average measured sensitivity of 2988.23 rad/(ε/s), the dynamic strain rate resolution at 1 kHz can be calculated as 1.58 nε/(s · √Hz).

The RINs of three PDs are tested and estimated. By performing ellipse fitting on any two of the three detections, the DC components, AC components, and θ of the three detections can be determined. The equivalent phase noise of RIN is calculated and shown in Fig. 4 with a red line. The equivalent phase noise of RIN is close to the measured phase noise floor, with a difference of ∼5 dB between 100 Hz and 10 kHz. At 1 kHz, the equivalent phase noise of RIN is −111 dB. Using the measured sensitivity of 2988.23 rad/(ε/s), the strain rate resolution limited by the RIN is 0.94 nε/(s · √Hz), which is close to the measured dynamic resolution of 1.58 nε/s. Therefore, reducing RIN is the main way to improve the resolution of the proposed FOSRS.

Furthermore, we explore the static resolution of the FOSRS. The output phase in 10 min is recorded. Since we are interested in static strain rate measurement, low-pass filtering with a cutoff frequency of 1 Hz is used to process the recorded phase. The result is shown in Fig. 5. The standard deviation of the recorded phase is calculated to be 2.0192×10^{-5} rad. Using the average measured sensitivity, a static strain rate resolution of 6.76 nε/s is demodulated.

To validate the strain rate measurable ability of the FOSRS, a triangular-wave voltage with a frequency of 0.05 Hz and peak-to-peak value of 20 V is applied to the PZT. Theoretically, the strain of the sensing fiber wound on the PZT is also in the form of a triangle wave. Since the FOSRS measures the strain rate, it can measure the slope of the strain, which then displays the phase in the form of a rectangular wave. The result recorded in 200 s is shown in Fig. 6 (data are filtered between 0.04 and 8 Hz). The output phase is in a rectangular wave, and its root mean square (RMS) amplitude value is approximately 65 μrad. That is, the FOSRS can measure a strain rate signal of about 22 nε/s at a frequency of 0.05 Hz, implying that the proposed FOSRS has the ability for nε/s static strain rate measurement. Similar to some experimental results for the reported strain rate sensors [16,17,22], direct measurement of FOSRS can record a clear strain rate signal with a high SNR.

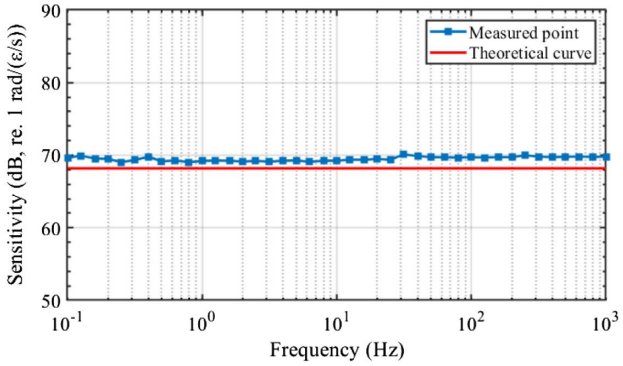

Fig. 3. Comparison of measured sensitivity and theoretical curve.

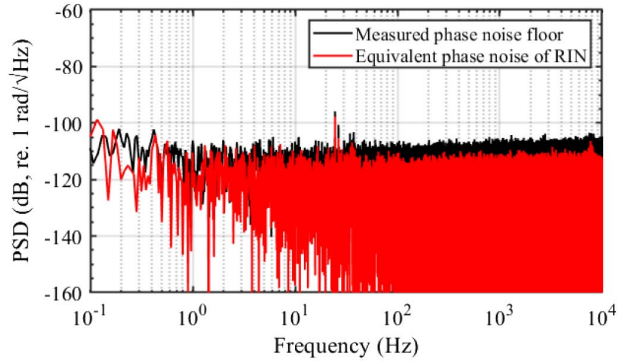

Fig. 4. Comparison of measured phase noise floor and equivalent phase noise of RIN.

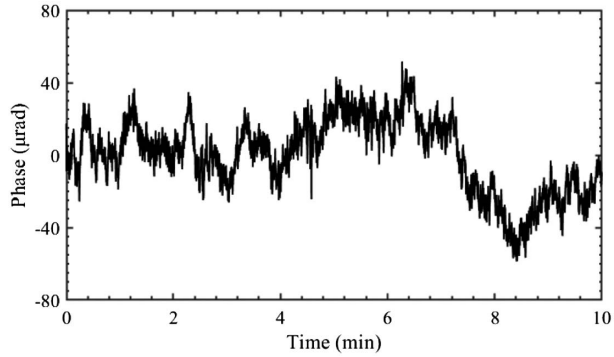

Fig. 5. Phase noise recorded for 10 min.

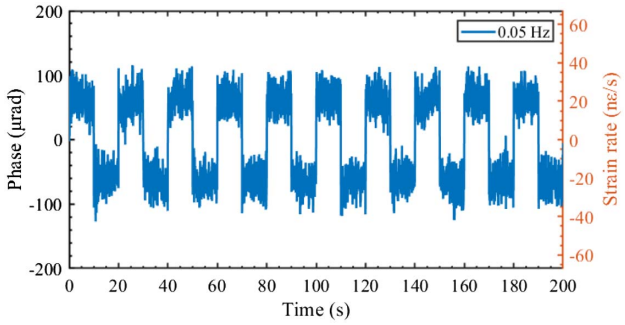

Fig. 6. Recorded rectangular signal of 0.05 Hz.

D. Dynamic Range Test

For the dynamic range in the dynamic strain rate measurement, the maximum measurable strain rate of the proposed FOSRS needs to be tested. When the THD of the signal at each frequency point reaches 10%, we take the corresponding phase on the PSD as the upper limitation of demodulation. Combined with the phase noise floor shown in Fig. 4, the dynamic range can be calculated and is shown in Fig. 7. The higher the signal frequency is, the smaller the dynamic range of the FOSRS. The THD can be suppressed with better algorithms such as ellipse fitting [30] to further improve the dynamic range.

In static strain rate measurement, the dynamic range of the FOSRS can be evaluable. Through Eq. (15), the maximum measurable strain rate can be calculated as ~0.1 ε/s. According to data from Corning Inc., the optical fiber can be loaded with an applied stress of 700 MPa within 7 ms, indicating that it can withstand a strain rate amplitude of at least 1.42 ε/s. Therefore, in static measurement, the maximum measurable strain rate is approximately 0.1 ε/s. Combined with the above static strain rate resolution of 6.76 nε/s, the dynamic range of the proposed FOSRS is up to 140 dB.

E. Long Baseline Sensing

In the field of geophysical monitoring and crustal deformation observation, long baseline instruments have the advantages of ultrahigh resolution and the ability to average the noise from localized effects [31]. Therefore, FOSRS with a sensing fiber length of 25.277 km is developed. First, we disconnect the optical fiber between the PZT and the 1 × 2 coupler. Then, we splice an optical fiber disk with a length of 25.277 km at the output end of the 1 × 2 coupler, and finally we splice an FRM to the end of the sensing fiber. To differentiate the FOSRS with different sensing fibers, the FOSRS with a 12.1 m sensing fiber and 4.653 km delay fiber is called FOSRS I, and the FOSRS with a 25.277 km sensing fiber and 4.653 km delay fiber is called FOSRS II.

FOSRS II is placed in the same testing environment as FOSRS I. The phase noise floor of FOSRS II is tested and shown in Fig. 8. The recorded phase is filtered by a low-pass filter with a cutoff frequency of 1 Hz. Compared to the result of FOSRS I, FOSRS II has higher noise. This is due to the longer sensing fiber, which increases the sensitivity of FOSRS II and makes it more sensitive to ambient noise, such as the effect of temperature. To reduce the effect of temperature in practical applications, it is possible to use a reference interferometer, whose arm length difference is equal to the length of the sensing fiber, to eliminate the temperature variation trend. Also, the use of long sensing fibers significantly increases the thermal phase noise introduced by random thermal fluctuations in the optical fibers [32–34], resulting in a significant increment in the phase noise of FOSRS II.

The recorded phase's standard deviation is calculated to be 9.1180×10^{-5} rad. Because of the longer length of the sensing fiber, the sensitivity of FOSRS II is difficult to calibrate. However, according to the above study on FOSRS I, its measured sensitivity is close to its theoretical sensitivity, and the difference between them is permissible. Therefore, the theoretical value is adopted as the sensitivity of FOSRS II. Using a theoretical sensitivity of 5.36×10^{6} rad/(ε/s), a static strain rate resolution of 17.01 pε/s is obtained.

In Table 2, we compare the resolution of the FOSRS with some strain rate values of the DAS. The strain rate of the DAS is calculated by measuring the relative deformation and time difference over the gauge length by demodulating the phase change of the backscattered light. The length of the sensing fiber corresponds to the gauge length of the DAS. From Table 2, the resolution of the FOSRS can be better than the noise of the DAS. Considering the strain rate amplitudes detected by DAS in volcano monitoring and microseism detection, it is shown that the FOSRS is suitable for geophysical monitoring and the detection of seismic events.

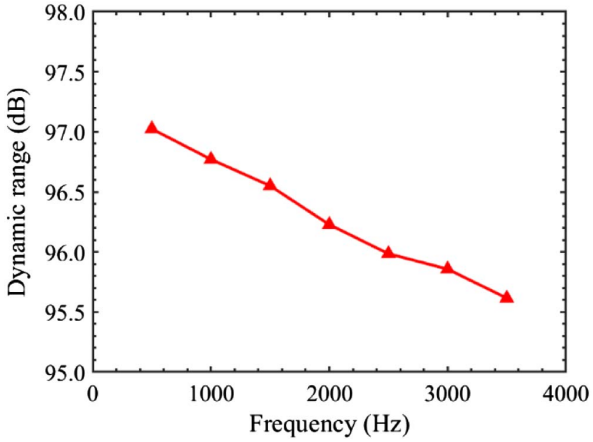

Fig. 7. Dynamic range for dynamic measurement.

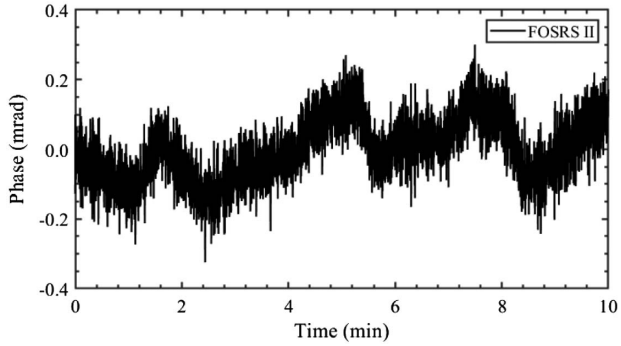

Fig. 8. Phase noise of FOSRS II recorded over 10 min.

Table 2. Comparison of FOSRS and DAS

Reference	Gauge Length	Description	Value (nε/s)
[13]	10 m	Noise RMS of DAS	90
[15]	10 m	Small transients within the persistent volcanic tremor	5
[35]	10 m	Stick-slip icequake in glaciated terrain	649
FOSRS I	12.1 m	Dynamic/static resolution	1.58/6.76
FOSRS II	25.277 km	Static resolution	0.017

4. CONCLUSION

An FOSRS based on a differentiating MZI is proposed, and its performance is researched in detail. A sensing fiber is used to directly measure the strain rate with the help of the differentiating interferometer. The flat sensitivity of the developed FOSRS with a 12.1 m sensing fiber is 69.50 dB between 0.1 Hz and 1 kHz. A dynamic strain rate resolution of 1.58 nε/s at 1 kHz and a static strain rate resolution of 6.76 nε/s in 10 min are obtained. The resolution is limited by the RIN of the ASE light source. In the static measurement, the maximum measurable strain rate that is limited by the coherence length of the light source is approximately 0.1 ε/s, and the corresponding dynamic range is evaluated as 140 dB. FOSRS with a longer sensing fiber has a higher sensitivity and resolution but is also limited by thermal noise and high sensitivity to ambient noise. A 25.277 km sensing fiber is used to achieve an ultrahigh static resolution of 17.07 pε/s. We believe that FOSRS, with its advantages of flat sensitivity, high resolution, and large dynamic range, has potential in geophysical monitoring and crustal deformation observation.

APPENDIX A

The 3×3 coupler is neither lossless nor symmetrical in actual measurements. When no strain rate signal is measured, the three detection optical powers in Eq. (11) should be described as

$$\begin{aligned} P_1 &= D_1 + A_1\cos(\theta_0),\\ P_2 &= D_2 + A_2\cos(\theta_0+\theta_1),\\ P_3 &= D_3 + A_3\cos(\theta_0+\theta_2), \end{aligned} \tag{A1}$$

where $D_1/A_1 \neq D_2/A_2 \neq D_3/A_3$, $|\theta_1| \neq |\theta_2| \neq 2\pi/3$, and θ_0 is the initial phase.

RIN comes from the broadband light source and is divided into three parts after passing through a 3×3 coupler, entering three PDs. Three RINs tested from three PDs are not exactly equal and correlated. The intensity noise related to the RINs can be expressed by

$$n_{\mathrm{RIN}} = \left[10^{\frac{\mathrm{RIN1}}{20}} \quad 10^{\frac{\mathrm{RIN2}}{20}} \quad 10^{\frac{\mathrm{RIN3}}{20}}\right]^T. \tag{A2}$$

In the FOSRS, due to the performance of the 3×3 coupler and the arctangent algorithm, the variance of the equivalent phase noise of the RIN is [36]

$$\sigma^2_{\mathrm{RIN}} = p^T_{\theta_0} P n_{\mathrm{RIN}} n^T_{\mathrm{RIN}} P p_{\theta_0}. \tag{A3}$$

Here,

$$P = \begin{bmatrix} P_1 & 0 & 0\\ 0 & P_2 & 0\\ 0 & 0 & P_3 \end{bmatrix}, \tag{A4}$$

$$p^T_{\theta_0} = p^T\cos\theta_0 - q^T\sin\theta_0, \tag{A5}$$

$$\begin{bmatrix} q^T\\ p^T \end{bmatrix} = \frac{\begin{bmatrix} \frac{A_3}{A_1}\frac{D_2}{D_1}\sin\theta_2 - \frac{A_2}{A_1}\frac{D_3}{D_1}\sin\theta_1 & -\frac{A_3}{A_1}\sin\theta_2 & \frac{A_2}{A_1}\sin\theta_1\\ \frac{A_3}{A_1}\frac{D_2}{D_1}\cos\theta_2 - \frac{A_2}{A_1}\frac{D_3}{D_1}\cos\theta_1 & \frac{D_3}{D_1} - \frac{A_3}{A_1}\cos\theta_2 & \frac{A_2}{A_1}\cos\theta_1 - \frac{D_2}{D_1} \end{bmatrix}}{\frac{D_2}{D_1}A_3\sin\theta_2 - \frac{D_3}{D_1}A_2\sin\theta_1 + \frac{A_2}{A_1}A_3\sin(\theta_1-\theta_2)}. \tag{A6}$$

Furthermore, the PSD of the equivalent phase noise of the RIN is

$$\begin{aligned} \psi_{\mathrm{RIN}} = 10\lg\Big(&p^2_{\theta_0 1}P_1^2 10^{\frac{\mathrm{RIN1}}{10}} + p^2_{\theta_0 2}P_2^2 10^{\frac{\mathrm{RIN2}}{10}} + p^2_{\theta_0 3}P_3^2 10^{\frac{\mathrm{RIN3}}{10}}\\ &+ 2p_{\theta_0 1}p_{\theta_0 2}P_1P_2 10^{\frac{\mathrm{RIN1+RIN2}}{20}} + 2p_{\theta_0 2}p_{\theta_0 3}P_2P_3 10^{\frac{\mathrm{RIN2+RIN3}}{20}}\\ &+ 2p_{\theta_0 3}p_{\theta_0 1}P_3P_1 10^{\frac{\mathrm{RIN3+RIN1}}{20}}\Big). \end{aligned} \tag{A7}$$

By fitting the ellipse and calibrating D_1/A_1, D_2/A_2, D_3/A_3, θ_1, and θ_2, the corresponding equivalent phase noise can be obtained. Moreover, it is foreseeable that the equivalent phase noise of RIN is affected by the change of the initial phase. In the resolution limitation and noise analysis of this paper, we take the equivalent phase noise when the initial phase is zero.

Funding. National Natural Science Foundation of China (61875185, U1939207); Scientific Instrument Developing Project of the Chinese Academy of Sciences

(YJKYYQ20210036); Shenzhen Science and Technology Planning Project (JCYJ20190814110601663).

Acknowledgment. H. C. Li proposed the method, performed the experiment, analyzed the data, and wrote the draft of the paper; W. Z. Huang edited the paper and assisted in processing the data; J. X. Zhang assisted in demodulating the sensor; W. T. Zhang revised the manuscript and supervised the project.

Disclosures. The authors declare no conflicts of interest.

Data Availability. Data underlying the results presented in this paper are not publicly available at this time but may be obtained from the authors upon reasonable request.

REFERENCES

1. J.-W. Baek, H.-K. Yang, and H.-G. Park, "Loading rate effect on reinforced concrete walls with low aspect ratios under high-frequency earthquake," ACI Struct. J. **117**, 105–118 (2020).
2. W. Wang, "Strain rate effect on the progressive collapse analysis of RC frame structure under earthquake," Adv. Civ. Eng. **2020**, 5808701 (2020).
3. H. Zhang and H. N. Li, "Dynamic analysis of reinforced concrete structure with strain rate effect," Mater. Res. Innov. **15**, S213–S216 (2011).
4. M. Li and H. Li, "Effects of strain rate on reinforced concrete structure under seismic loading," Adv. Struct. Eng. **15**, 461–475 (2012).
5. F. Masson, J. Chéry, D. Hatzfeld, J. Martinod, P. Vernant, F. Tavakoli, and M. Ghafory-Ashtiani, "Seismic versus aseismic deformation in Iran inferred from earthquakes and geodetic data," Geophys. J. Int. **160**, 217–226 (2005).
6. V. L. Stevens and J.-P. Avouac, "On the relationship between strain rate and seismicity in the India–Asia collision zone: implications for probabilistic seismic hazard," Geophys. J. Int. **226**, 220–245 (2021).
7. E. Hussain, T. J. Wright, R. J. Walters, D. P. S. Bekaert, R. Lloyd, and A. Hooper, "Constant strain accumulation rate between major earthquakes on the North Anatolian fault," Nat. Commun. **9**, 1392 (2018).
8. E. Gunawan and S. Widiyantoro, "Active tectonic deformation in Java, Indonesia inferred from a GPS-derived strain rate," J. Geodyn. **123**, 49–54 (2019).
9. A. Dogru, "Deformation of Eastern Turkey from seismic and geodetic strain rates," Sci. Res. Essays **5**, 911–916 (2010).
10. M. Hackl, R. Malservisi, and S. Wdowinski, "Strain rate patterns from dense GPS networks," Nat. Hazards Earth Syst. Sci. **9**, 1177–1187 (2009).
11. J. Wang, "Calculation method of strain rate field based on GPS observation," Earthquake **39**, 122–134 (2019).
12. I. Lior, A. Sladen, D. Mercerat, J.-P. Ampuero, D. Rivet, and S. Sambolian, "Strain to ground motion conversion of distributed acoustic sensing data for earthquake magnitude and stress drop determination," Solid Earth **12**, 1421–1442 (2021).
13. H. F. Wang, X. Zeng, D. E. Miller, D. Fratta, K. L. Feigl, C. H. Thurber, and R. J. Mellors, "Ground motion response to an ML 4.3 earthquake using co-located distributed acoustic sensing and seismometer arrays," Geophys. J. Int. **213**, 2020–2036 (2018).
14. S. Ide, E. Araki, and H. Matsumoto, "Very broadband strain-rate measurements along a submarine fiber-optic cable off Cape Muroto, Nankai subduction zone, Japan," Earth Planets Space **73**, 63 (2021).
15. P. Jousset, G. Currenti, B. Schwarz, A. Chalari, F. Tilmann, T. Reinsch, L. Zuccarello, E. Privitera, and C. M. Krawczyk, "Fibre optic distributed acoustic sensing of volcanic events," Nat. Commun. **13**, 1753 (2022).
16. C. K. Lee and T. C. O'Sullivan, "Piezoelectric strain rate gages," J. Acoust. Soc. Am. **90**, 945–953 (1991).
17. J. Juston and D. Bauer, "Strain rate sensing for vibration control of flexible structures," in *32nd Structures, Structural Dynamics, and Materials Conference* (1991), paper AIAA 1991-1118.
18. P. Costa Antunes, J. Miguel Dias, H. Varum, and P. André, "Dynamic structural health monitoring of a civil engineering structure with a POF accelerometer," Sens. Rev. **34**, 36–41 (2014).
19. M. A. Zumberge, W. Hatfield, and F. K. Wyatt, "Measuring seafloor strain with an optical fiber interferometer," Earth Space Sci. **5**, 371–379 (2018).
20. Q. Liu, Z. He, and T. Tokunaga, "Sensing the earth crustal deformation with nano-strain resolution fiber-optic sensors," Opt. Express **23**, A428–A436 (2015).
21. T. Chang, Y. Yang, Z. Luo, M. Yu, Y. Yuan, F. Yu, and H.-L. Cui, "Shallow seafloor seismic wave monitoring using 3-component fiber optic interferometric accelerometer," Meas. Sci. Technol. **33**, 015101 (2021).
22. Y. L. Lo and J. S. Sirkis, "Strain-rate sensor based on in-fiber Doppler velocimetry," Opt. Eng. **37**, 1648–1654 (1998).
23. C. D. Butter and G. B. Hocker, "Fiber optics strain gauge," Appl. Opt. **17**, 2867–2869 (1978).
24. S. J. Spammer and P. L. Swart, "Differentiating optical-fiber Mach–Zehnder interferometer," Appl. Opt. **34**, 2350–2353 (1995).
25. M. Born and E. Wolf, *Principles of Optics: Electromagnetic Theory of Propagation, Interference and Diffraction of Light*, 7th ed. (Cambridge University, 1999).
26. X. Chen, M. Yan, J. Yu, and R. Tang, "Design of light source for ultra-high precision fiber optic gyroscope," Proc. SPIE **12062**, 1206211 (2021).
27. J. Honthaas, J.-J. Bonnefois, E. Ducloux, and H. Lefèvre, "Interferometric filtering of the excess relative intensity noise of the broadband source of a fiber optic gyroscope," Proc. SPIE **9157**, 91572D (2014).
28. R. C. Rabelo, R. T. d. Carvalho, and J. Blake, "SNR enhancement of intensity noise-limited FOGs," J. Lightwave Technol. **18**, 2146–2150 (2000).
29. S. Zhao, Q. Liu, Y. Liu, H. Ma, and Z. He, "Navigation-grade resonant fiber-optic gyroscope using ultra-simple white-light multibeam interferometry," Photon. Res. **10**, 542–549 (2022).
30. J. Zhang, W. Huang, W. Zhang, and F. Li, "Improved DFB-FL sensor interrogation with low harmonic distortion based on extended Kalman filter," J. Lightwave Technol. **39**, 5183–5190 (2021).
31. A. Araya, A. Takamori, W. Morii, K. Miyo, M. Ohashi, K. Hayama, T. Uchiyama, S. Miyoki, and Y. Saito, "Design and operation of a 1500-m laser strainmeter installed at an underground site in Kamioka, Japan," Earth Planets Space **69**, 77 (2017).
32. K. Krakenes and K. Blotekjaer, "Comparison of fiber-optic Sagnac and Mach-Zehnder interferometers with respect to thermal processes in the fiber," J. Lightwave Technol. **13**, 682–686 (1995).
33. L. Duan, "Thermal noise-limited fiber-optic sensing at infrasonic frequencies," IEEE J. Quantum Electron. **51**, 7700106 (2015).
34. Y. Li, Y. Cao, D. He, Y. Wu, F. Chen, C. Peng, and Z. Li, "Thermal phase noise in giant interferometric fiber optic gyroscopes," Opt. Express **27**, 14121–14132 (2019).
35. F. Walter, D. Gräff, F. Lindner, P. Paitz, M. Köpfli, M. Chmiel, and A. Fichtner, "Distributed acoustic sensing of microseismic sources and wave propagation in glaciated terrain," Nat. Commun. **11**, 2436 (2020).
36. H. Zhang, M. Zhang, L. Wang, Y. Liao, and D. N. Wang, "Output noise analysis of optical fiber interferometric sensors using a 3 × 3 coupler," Meas. Sci. Technol. **22**, 125203 (2011).